

Final Technical Report

Award Number: G14AP00071

Start and End Dates:

July 1, 2014 to January 31, 2016

UNDERSTANDING TRIGGERING OF REPEATED ASEISMIC STRAIN CHANGES IN THE ANZA GAP

Duncan Carr Agnew
Institute of Geophysics and Planetary Physics
Scripps Institution of Oceanography
University of California
La Jolla CA 92093-0225 USA
(858) 534-2590 (FAX 534-5332)
dagnew@ucsd.edu

February 16, 2017

Abstract

This grant supported the analysis of strainmeter and other data adjacent to the Anza segment of the San Jacinto fault, a seismic gap on which there has been increased numbers of moderate earthquakes over the last few years. We find that:

1. Following a magnitude 4.7 earthquake in the San Jacinto fault zone on March 11, 2013, rapid and very similar strain changes were observed on the long-base strainmeters (LSM's) at Piñon Flat Observatory (PFO), and on the borehole strainmeters (BSM's) installed there and elsewhere in the Anza region. The BSM and LSM's at PFO have no elements in common, which rules out instrumental problems and the similarity of the strains means that these must be uniform over distances of several km or more.
2. The pattern of strain change seen on the LSM's, with accelerated strain rates over periods of weeks, has also been observed after the 2005 Anza earthquake (magnitude 5.2, 21 km from PFO) and the 2010 Collins Valley earthquake (magnitude 5.4, 25 km), the 2010 El Mayor earthquake (magnitude 7.2, 185 km), the 2001 Anza earthquake (5.0, 21 km), the 1999 Hector Mine earthquake (7.1, 111 km), and the 1992 Joshua Tree earthquake (6.1, 44 km) – though not after the 1992 Landers event (7.3, 66 km), which caused a different kind of, and much larger, postseismic signal
3. Modeling of these repeated aseismic strain changes at PFO show them to be consistent with deep slip in the region of the Anza seismic gap.
4. Rapid strain changes (lasting a few hours) seen on the LSM's and BSM's following the 2013 earthquake have also been repeatedly observed between 2007 and 2014 on these same instruments, showing a consistent pattern of relative strain. However, almost all of these events occur during daylight hours, and the vast majority on weekends. We therefore believe them to be the effect of local groundwater pumping, though we have not been able to identify the (now absent) source.

1 Introduction

The purpose of this project was to analyze deformation data along the Anza segment of the San Jacinto fault to improve our understanding of strain changes, most especially rapid and apparently aseismic variations seen on strainmeter data, largely from the long-base strainmeters (LSM's) at Piñon Flat Observatory (PFO). Because these instruments are located close to the section of the San Jacinto fault that has been longest without a large earthquake (the “Anza slip gap”) such transients are of even greater interest. Wdowinski (2009) has suggested that on the San Jacinto fault the transition from earthquakes to creep below the seismogenic zone is relatively shallow; such creep could well include unsteady as well as secular behavior.

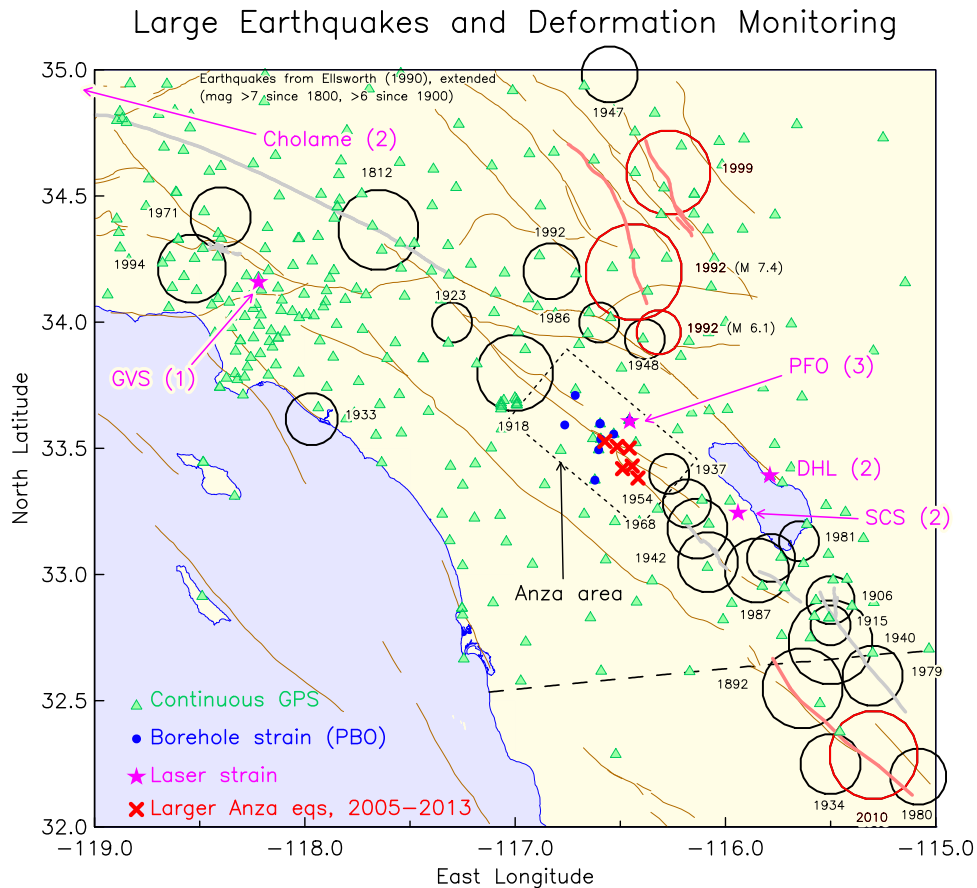


Figure 1: Large earthquakes and fault ruptures in southern California, with locations of laser strainmeters. Earthquakes discussed in this proposal are in red. The dashed box is the region shown in Figure 2.

Figure 1 shows large earthquakes, and deformation sensors, in Southern California. The San Jacinto fault has been ruptured by at least eight moderate earthquakes of magnitude 6 or larger since 1899; but, as originally noted by Thatcher *et al.* (1975) and Sanders and Kanamori (1984), the part of the fault near the town of Anza is the one exception: the “Anza seismic gap”. The slip rate for the fault is at least 10 mm/yr; paleoseismic results (Rockwell *et al.*, 2006; Salisbury *et al.*, 2012) show an average

Anza Seismicity, 2005–2016

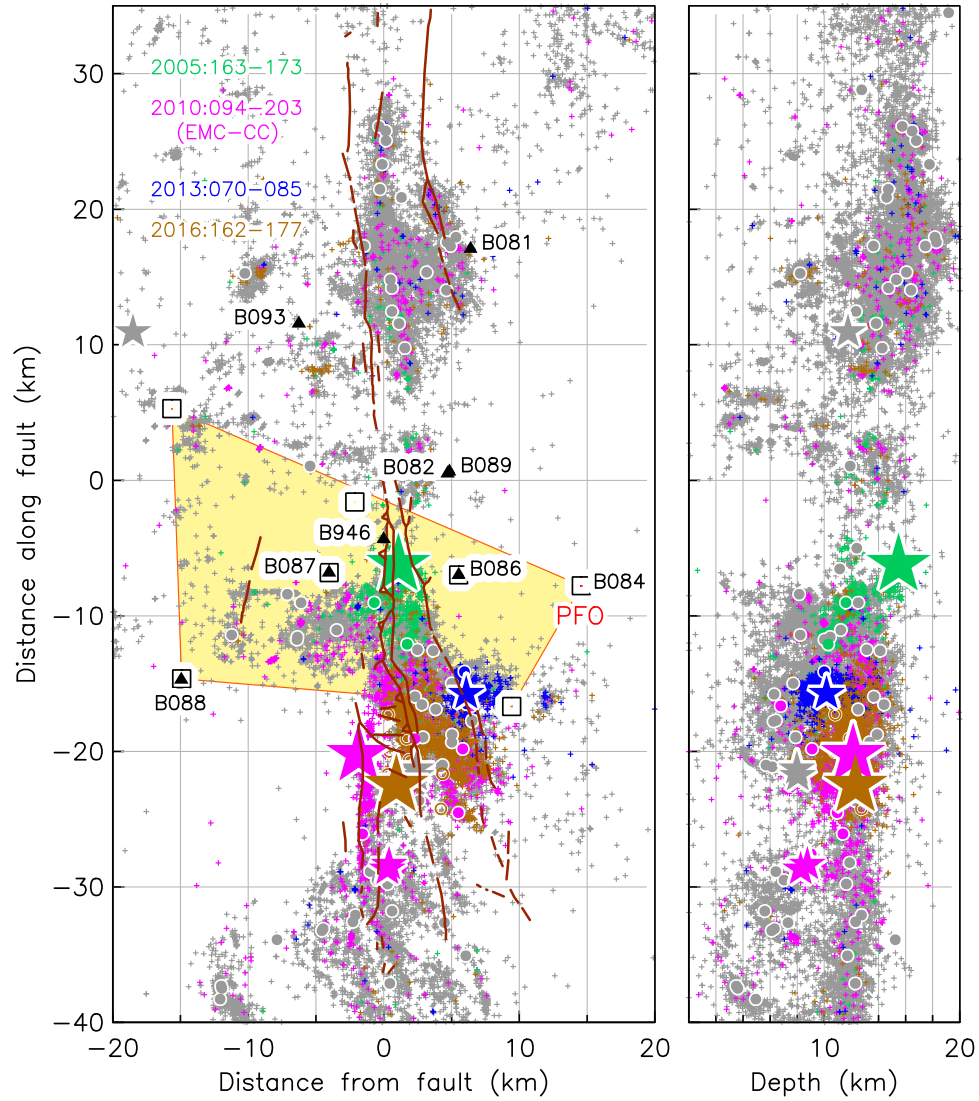


Figure 2: Seismicity (mag 0.5 and above, 2005-2016) along the Anza part of the San Jacinto fault, in map view and profile, using relocated hypocenters from Hauksson *et al.* (2012), plus SCSN after 2015.0. Particular sequences are shown in color. The locations of locations of the PBO borehole strainmeters (labeled) and GPS (squares) are shown; the yellow region is that covered by the GPS network analyzed in Figure 9.

repeat time of 250 yr, with the last event (magnitude 7.2 or more) more than 200 yr ago. Figure 2 shows the recent seismicity in this section in more detail. The maximum depth of seismicity deepens from southeast to northwest; the region where the fault trace is simplest, near Anza, is essentially aseismic, forming a seismicity gap within the slip gap

2 The Toro Peak Earthquake of March 11, 2013

Over the nearly 50 years from 1938 through 1996, the Anza region experienced six shocks with $M > 4.5$, and only one with $M > 5.0$: the Horse Canyon earthquake, $M 5.3$, 1980:056. In the 19 years from 1997 there have been seven shocks above magnitude 4.5, four with $M \geq 5.0$, all shown on Figure 2. The event at 2013:070:16:56 was a magnitude 4.7 earthquake whose epicenter was 12 km south of PFO with a depth of 9 km, so the hypocenter distance is 15 km. The high-frequency accelerations from this event caused the LSM's to lose fringe lock briefly, so we do not have an estimate of the coseismic offset; but this outage lasted less than a minute.

Combining the NS and EW LSM records to form two of the strains usually computed for the BSM's showed fairly good agreement between these and the strains recorded by the BSM at PFO, B084. As shown in Figure 16, this borehole sensor lies within the region covered by the LSM's. The agreement is best for the γ_1 shear (the shear parallel to a NWSE-striking fault) and the areal strain e_a . The γ_2 strains do not match very well, though this may reflect an inaccurate calibration of the BSM. The strains shown in Figure 3 (except in the lower right panel) are all derived from combinations of sensors; for shear this reduces common-mode noise in the BSM's, though combining the LSM's often increases the apparent noise over that of an individual sensor.

The NS and EW LSM's at PFO share nothing except their source of power (line power), though for most of the subsystems in these instruments even this is passed through separate uninterruptible power supplies. And the BSM is completely independent of the LSM's in everything from power (the BSM runs on batteries charged from line power) to telemetry (BSM data is collected directly by PBO). Instrument misbehavior can thus be ruled out: these deformations have to actually be in the ground. The LSM's do share with each other, and with the BSM electronics, exposure to weather changes: but the period after the earthquake was in fact one of very benign weather, with no rain or large air pressure changes – just the regular daily cycle of sunshine and temperature. We monitor line voltage and current coming into PFO, and these also showed no unusual changes.

Even more interesting, a closer look at the data showed several “events”: intervals of especially high strain rates, again coinciding on both the NS and EW LSM's and on the BSM. Figure 4 shows the first two events after the earthquake; there were others over the next few days. None of these coincided with unusual environmental fluctuations. We initially examined BSM and LSM data for some days prior to the earthquake, and also over several earlier months, and did not see anything similar to these episodes; but a more thorough search (Section 7) did reveal more, as well as showing that these are very unlikely to be tectonic in origin.

Additional data comes from the other BSM's installed by the PBO in the Anza region, and the other LSM's shown in Figure 1. Of the BSM's shown in Figure 2, B082 and B089 are badly affected by

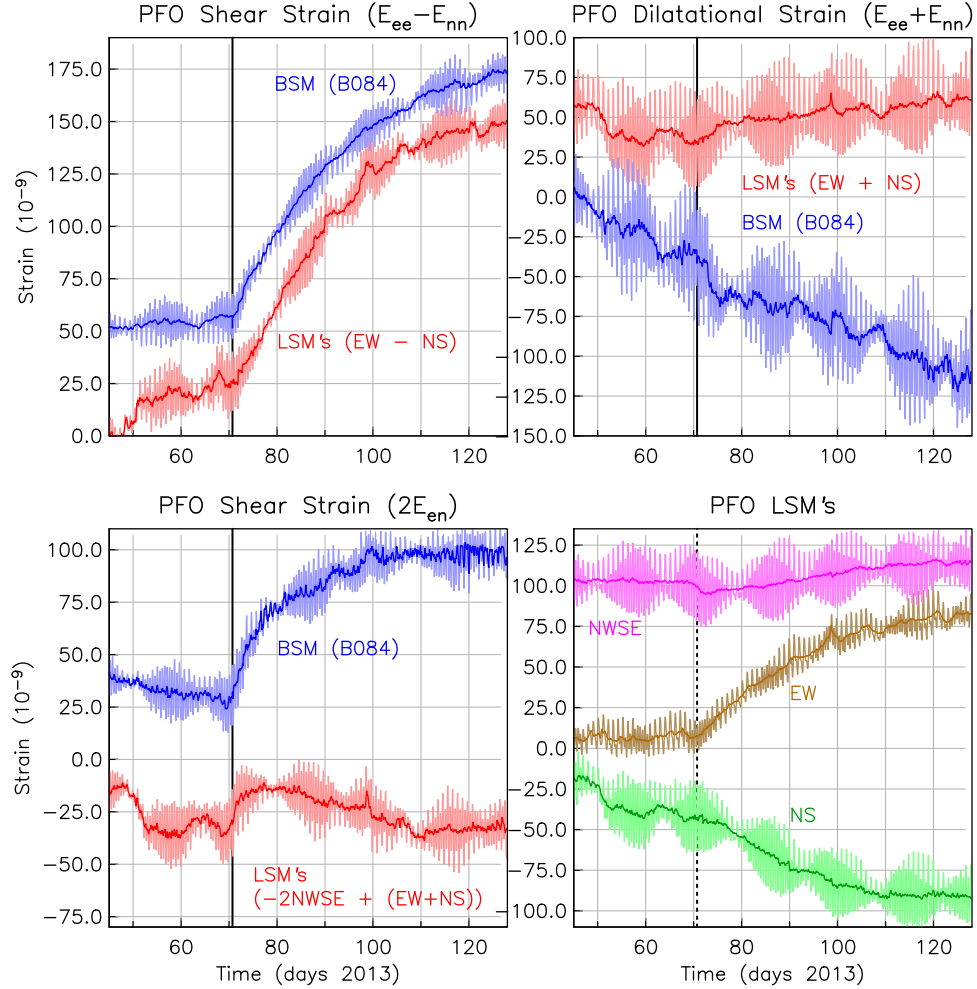


Figure 3: Comparison of two components of shear, and the areal strain, at PFO, showing the post-seismic behaviors of the LSM's and BSM's after the Toro Peak earthquake (dashed black line). The BSM data are detrended; the LSM data are not. Data are shown with and without tides; in the detided records K_1 and K_2 variations have been removed from the BSM areal strain and all the LSM data. The BSM calibration of Hodgkinson *et al.* (2013) was used. The lower right panel shows the individual LSM records.

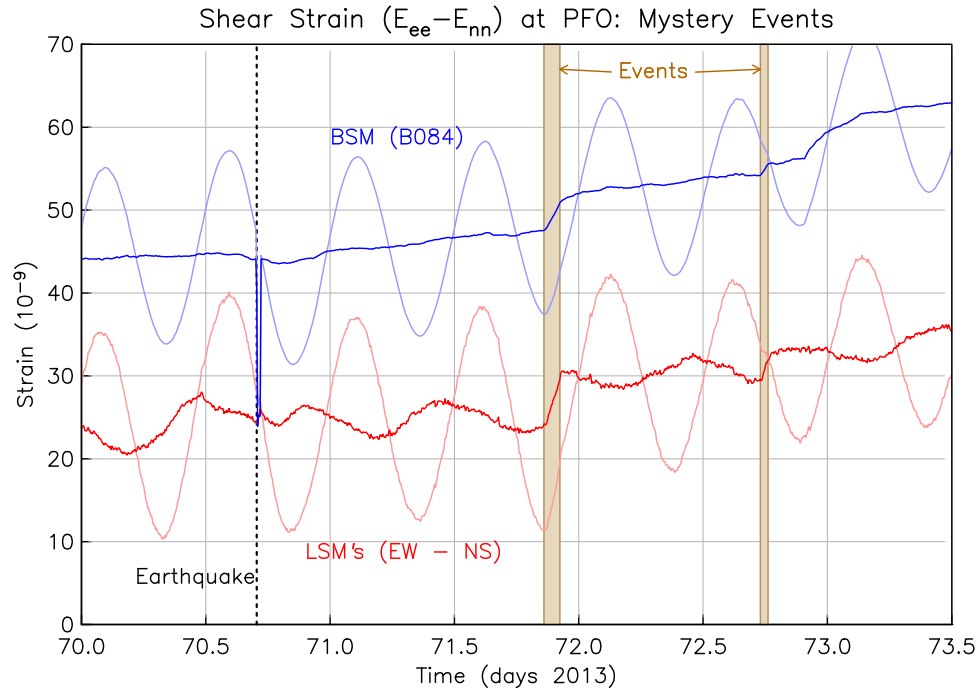


Figure 4: Detail of the shear on the PFO BSM and LSM, showing two rapid strain changes seen on both instruments: the first is over the time interval 71:20:39-22:11 and the second over 72:17:31-18:16.

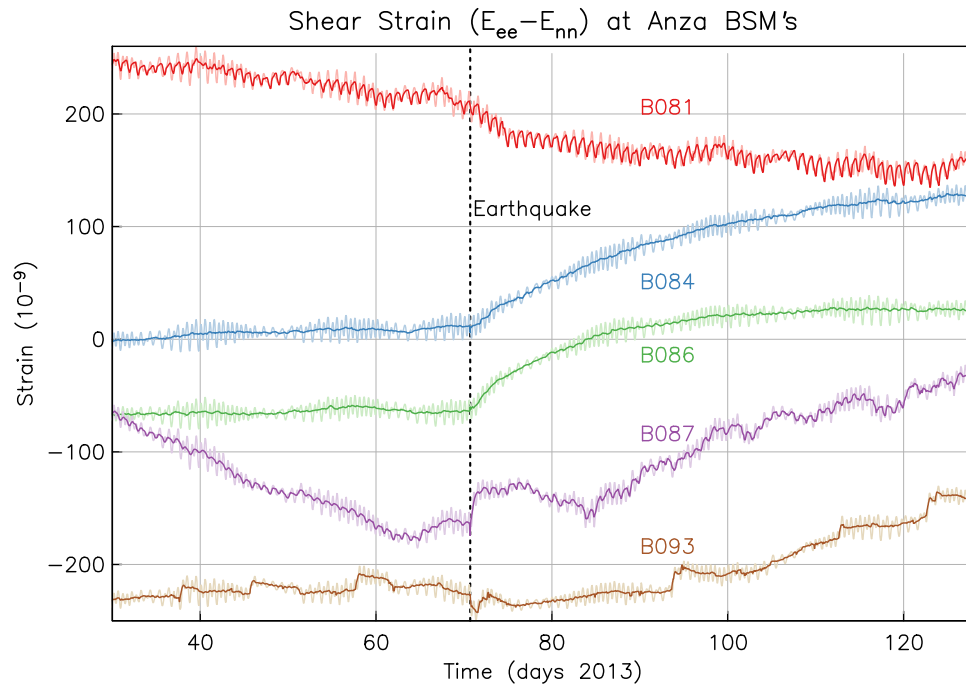


Figure 5: Fault-parallel shear from Anza BSM's, using the fully-corrected PBO time series.

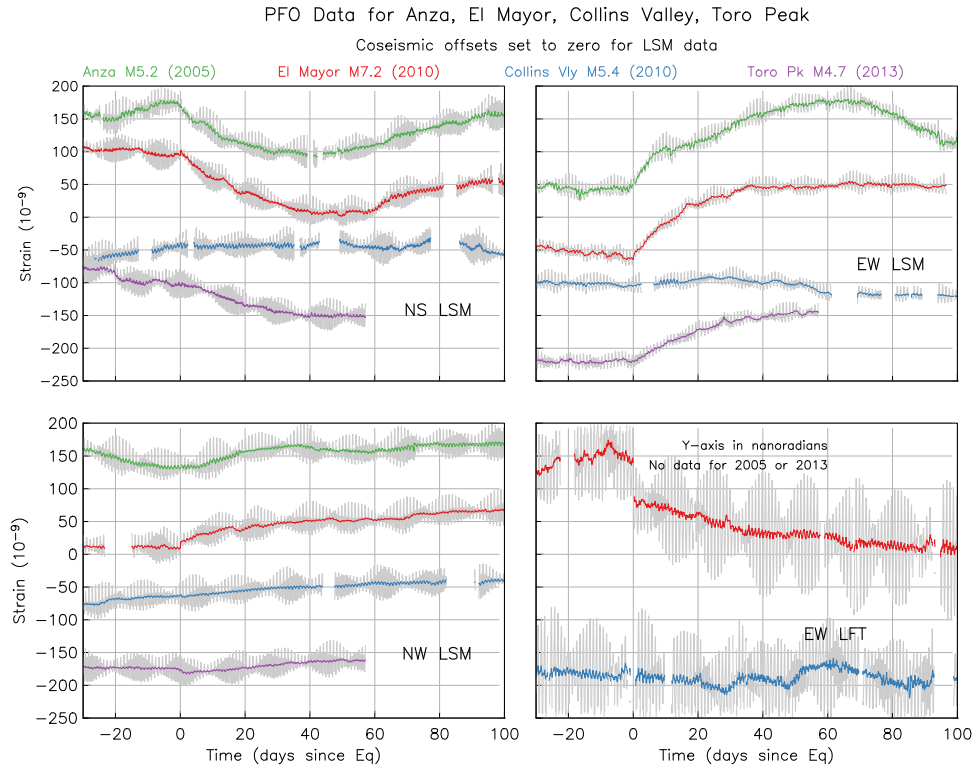


Figure 6: Response of the PFO LSM's to four earthquakes, one of which (the large local “Collins Valley” shock) caused a much smaller postseismic signal.

local pumping, and B088 and B946 showed very unstable behavior before the earthquake. Figure 5 shows estimated γ_1 strain (again, subject to calibration uncertainties) for B081, B084 (again), B086, B087, and B093. Some of these instruments show the same decaying postseismic signal seen at PFO, though not all do: of course, for a localized source (such as slip on a patch of the fault) they would not be expected to. We do not see any kind of signal related to the Toro Peak earthquake on the more distant LSM's. Also, we have not found any indication of the rapid postseismic strain events seen in Figure 4 on any strainmeter located elsewhere.

3 Previous Triggered Strains

Similar aseismic strain episodes had occurred before, after the 2005 Anza earthquake and the 2010 El Mayor Cucapah (EMC) earthquake (Figure 6). After the EMC earthquake all three PFO strainmeters started by showing postseismic strains that were roughly consistent, in size and shape, with their source being afterslip on the just-ruptured EMC fault: the signals were of the same sign, and larger on the NWSE and the EW than on the NS. But soon after, the strain rate on the NS changed sign, while that on the NWSE fell to near zero. In our view Figure 6 makes a convincing case for similar behavior, with the NS and EW LSM's showing roughly equal and opposite signals, decaying over several weeks, after three earthquakes: two local (2005 and 2013) and one more distant. But it also

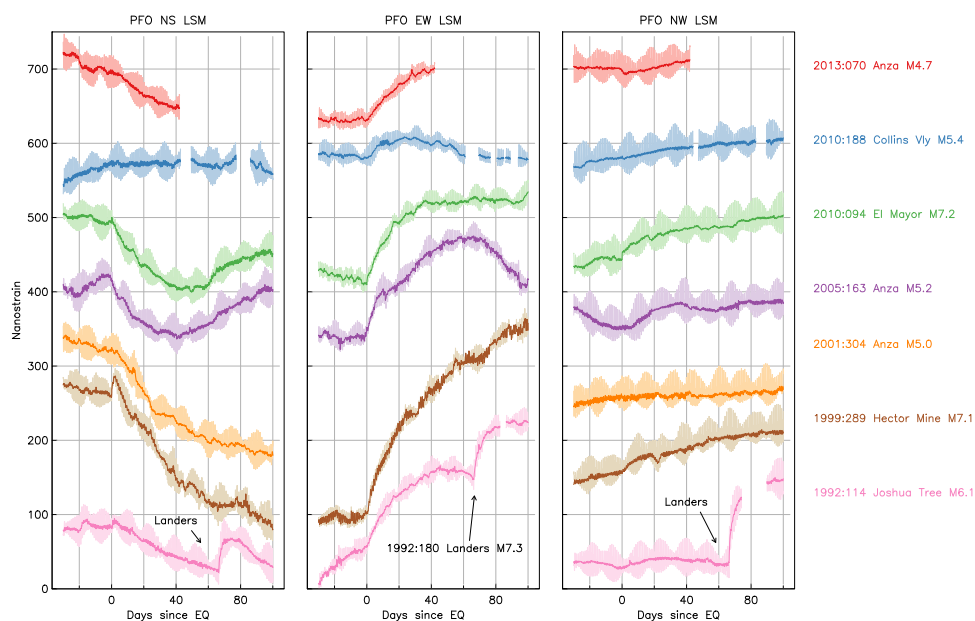


Figure 7: Responses of the three PFO LSM's to eight earthquakes, four local and four regional (see Table 1 for information).

shows a local earthquake that produced strong shaking at PFO but much smaller strain changes: the 2010 Collins Valley earthquake (Table 1).

In 2002-2003 the EW strainmeter was upgraded by adding optical anchors at both ends; prior to this time the only “anchoring” was provided by correcting the end pier tilts (this is still the method used at one end of the NS LSM). For this reason, prior to 2004 we put much more weight on the behavior of the fully-anchored NWSE instrument than on the other two, at least for longer-term changes. But, as Figure 6 shows, the postseismic response of the NWSE instrument seems to be – nothing. So after other earthquakes, whether moderate and local or large and regional, we had not examined the behavior of the other LSM's in detail. It has turned out, to our surprise, that the pattern seen since 2005 has occurred three other times: after the 1992 Joshua Tree, 1999 Hector Mine, and 2001 Anza earthquakes; Figure 7 shows the data. The 1992 Landers earthquake also produced a postseismic response, though a very different one (also shown in Figure 7): there appears to be a repeated pattern of strain change following either moderate local shocks or larger and more distant ones. In Section 6 we discuss how to interpret this.

4 Long-term Strain Changes at PFO

To set the most recent strain episodes into context, Figure 8 shows data from all three LSM's at PFO from 2008:274 through 2017:023. The postseismic responses to the EMC, Collins Valley, Toro Peak, and 2016 Borrego shocks are visible. And so is a large, year-long compressional strain starting in late 2010. This is quite unusual in terms of previous records, especially for the EW strainmeter, which

Table 1: Ground Motion at PFO

Date	Mag	Dist (km)	Pk. Acc. (cm ² /s)			Pk Vel (cm/s)			Name
			N	U	E	N	U	E	
1980:056	5.3	15.4	109	49	−124	−	−	−	Horse Canyon
1992:114	6.1	44.0	−	−	−	−	−	−	Joshua Tree
1992:180	7.3	66.1	25	−26	48	2.0	−5.2	2.9	Landers
1999:289	7.1	110.9	26	21	−35	−	−	−	Hector Mine
2001:304	5.0	21.1	−132	109	120	2.3	1.2	−3.6	Anza
2005:163	5.2	20.8	309	219	273	5.7	−3.5	7.3	Anza
2010:094	7.2	184.9	13	−14	13	−3.7	−2.4	−2.4	El Mayor
2010:188	5.4	24.6	182	−99	107	3.7	1.9	−2.2	Collins Vly
2013:070	4.7	15.4	−	−	−	−	−	−	Toro Pk

Table 1: Peak strong ground motion from earthquakes that caused strong shaking at PFO. – indicates that the information is not readily available, although we believe that strong-motion sensor data is available for all of these earthquakes.

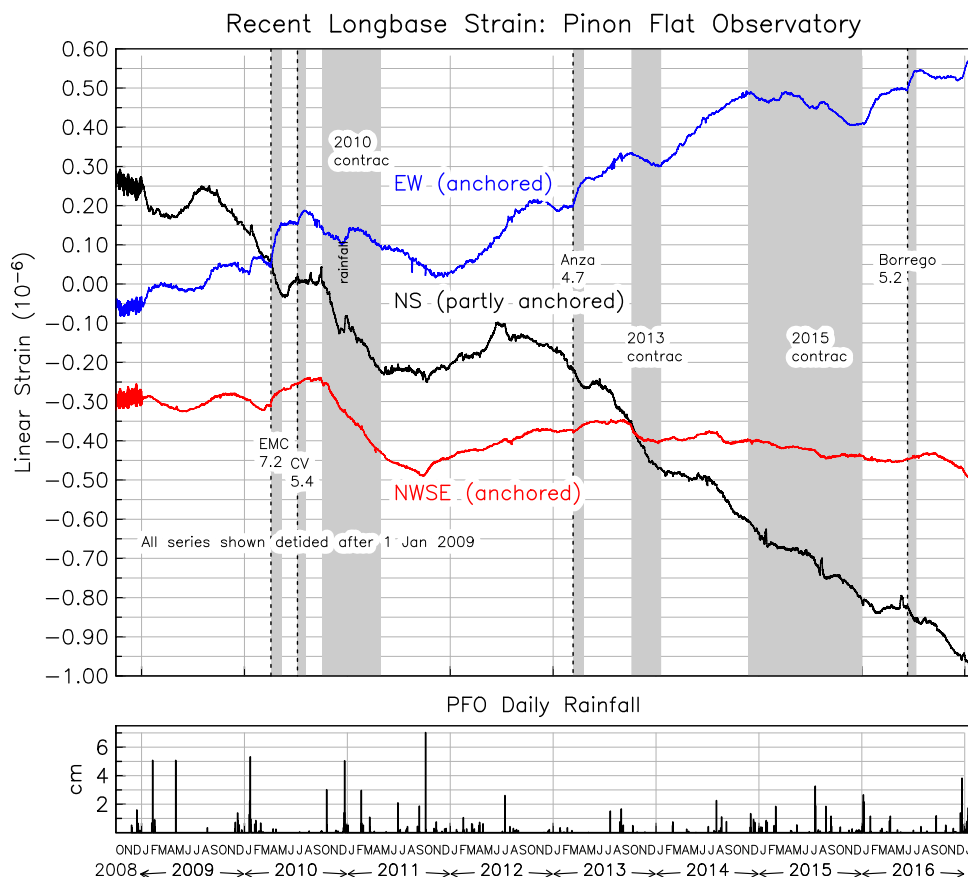


Figure 8: LSM data at PFO from late 2008 on. The gray regions labelled "contrac." are intervals during which the EW LSM has gone into contraction, against its own long-term trend.

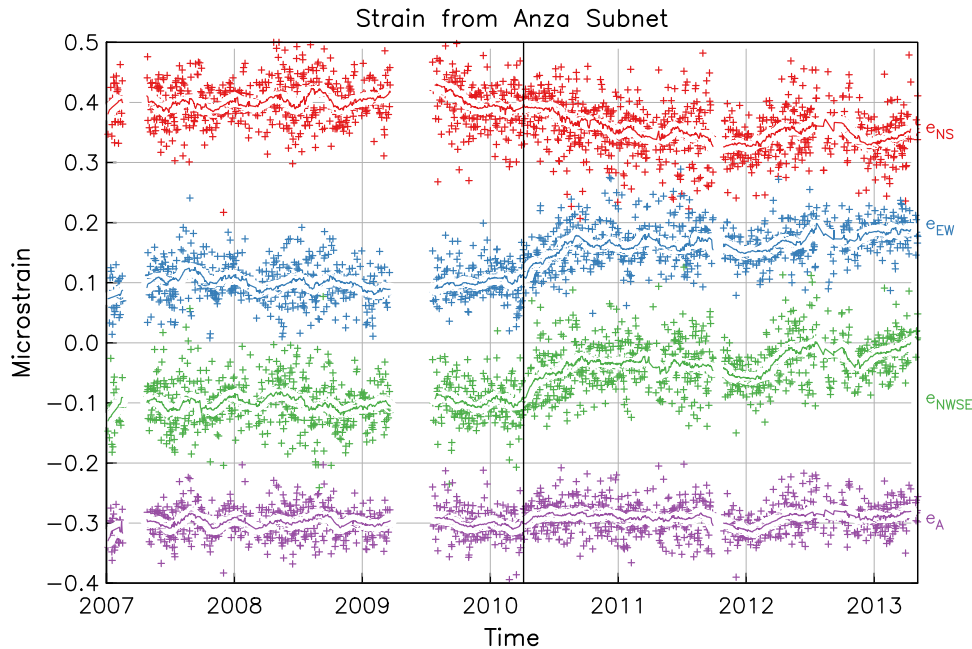


Figure 9: Strains computed from the displacements of continuous GPS stations AZRY, P479, P484, P490, P741, P742, and PIN1; the region covered is shown in Figure 2. For all, the secular trend before the EMC earthquake (black line) has been fit and removed; in $\mu\epsilon/\text{yr}$, these trends are -0.16 for NS strain, 0.14 for EW strain, 0.01 for NWSE strain, and 0.03 for dilatation. Daily results are shown as pluses, with a line used to show a smoothed result. The solid line is the time of the El Mayor earthquake.

generally shows (as it should) long-term extension; similar variations occurred in 2013 and 2015.

We have estimated a time series of strain in the Anza area using local CGPS stations (PBO and other; see Figure 9), and this shows a somewhat earlier, and different, long-term postseismic response to the EMC event. However, the GPS is averaging over a large area, and so is less sensitive to a locally-induced strain than the LSM's are. Unfortunately signals with this long a time constant are too slow to be reliably recovered from the BSM data.

5 Preliminary Interpretations

The question that has to be addressed first is whether the repeated signals we see at PFO – which are unquestionably ground deformation – are some kind of local response to strong shaking or large dynamic strains, or reflect tectonic motions. One thing we do know, at least for the most recent example, is that the PFO BSM data, basically a point measurement, is in good agreement with the LSM data. A hydrological change at the NW corner of PFO might well cause displacements of the LSM ends in that area; but it is highly improbable that this would displace the W and N ends in equal and opposite ways and the NW end not at all. This probability becomes vanishingly small if

such a localized source is also required to produce the same strains at the BSM, 400 m away and 150 m deep.

Indeed, the agreement of the LSM's and BSM at PFO imply that the strain, whatever its source, must have a scale length considerably greater than the LSM baselength of 720 m. It might be possible for an adjustment to the hydrology to have such a wavelength, though it is then difficult to see how it could have, in such relatively impermeable rocks, a time constant of only weeks. Even if this is possible, we have good evidence that the water table was not disturbed on this time scale, since neither the three water-level monitoring wells at PFO, nor the pore-pressure measurement made in the BSM borehole 32 m above the BSM, show any such changes.

Some evidence in favor of a hydrological effect may be provided by the results of Elkhoury *et al.* (2006), who showed that strong shaking at PFO usually resulted in a decrease in the phase lag of the tides in several of the water wells there, which they suggested was caused by increased permeability. The tidal phase would then gradually increase, perhaps because of a buildup of material in the fractures that provide most of the permeability at PFO. We have extended their tidal analysis to mid-2012, and find that the El Mayor shock produced a change in tidal phase close to the maximum size shown in Elkhoury *et al.* (2006). However, the 2010 Collins Valley earthquake (98 days after the El Mayor earthquake) which produced no postseismic strains, also does not appear to change the tidal phase. That this earthquake induced much smaller strains suggests that there may be some mechanism involved that does not respond if it has recently done so, something that seems equally plausible for either hydrological effects or triggered fault slip.

Arguing against an association is the fact that the recovery time for the tidal phase changes is often 1-2 years, much longer than the postseismic strains in Figure 7. Nor is it obvious how a small change in permeability alone (without changes in pore pressure) could produce such large, and irrecoverable, strain changes.

6 Slow Aseismic Strains: Modeling the Source

Putting aside the local interpretation for now, we examine the possibility that the postseismic signals were caused by aseismic slip on the San Jacinto fault. While it might not seem feasible to find the source of this slip from only three records, this turns out to be possible. For fault slip at a point, the ratio of observed strains does not vary, whatever the time history. Recognizing that we measure strain change, we denote the rate of strain on the i -th instrument (of N total) by $\dot{\epsilon}_i$. Define the unit vector $\hat{\mathbf{a}}(t)$ whose components are:

$$\hat{a}_i(t) = \frac{\dot{\epsilon}_i(t)}{(\sum_{i=1}^N (\dot{\epsilon}_i(t))^2)^{0.5}} \quad \text{for} \quad i = 1, \dots, N \quad (1)$$

Now consider slip $s(t)$ at location \mathbf{x} ; we expect that the strain rate on the i -th instrument will be given by

$$G_i(\mathbf{x})\dot{s}(t) \quad \text{for} \quad i = 1, \dots, N \quad (2)$$

Table 2

Event	Time d	Strain (10^{-9})		
		NS	EW	NWSE
Anza 2005	45	-70	120	30
EMC 2010	50	-100	100	50

Table 2: Postseismic strains following the 2005 Anza and 2010 El Mayor earthquake, estimated from Figure 7.

where \dot{s} is the slip rate at a location \mathbf{x} , and $G_i(\mathbf{x})$ is the Green function relating slip at location \mathbf{x} to predicted strain on the i -th instrument. Define a second unit vector $\hat{\mathbf{b}}(\mathbf{x})$ whose components are

$$\hat{b}_i(\mathbf{x}) = \frac{G_i(\mathbf{x})}{(\sum_{i=1}^N (G_i(\mathbf{x}))^2)^{0.5}} \quad \text{for } i = 1, \dots, N \quad (3)$$

If the strains are actually given by equation (2), then computing $\hat{\mathbf{a}}$ will give $\hat{\mathbf{b}}$; the slip rate $\dot{s}(t)$ in equation (2) will cancel, making $\hat{\mathbf{a}}$ and $\hat{\mathbf{b}}$ equal; since they are unit vectors, this amounts to saying that they will point in the same direction in N -dimensional space. Given an observed $\hat{\mathbf{a}}$, we can then find the misfit between this and the relative strains for slip at \mathbf{x} by finding the dot product of the two unit vectors, which gives us the angle between them. A suitable measure of misfit is

$$m(t, \mathbf{x}) = 1 - \arccos(\hat{\mathbf{a}} \cdot \hat{\mathbf{b}})$$

which will be zero when $\hat{\mathbf{a}}$ and $\hat{\mathbf{b}}$ have the same direction.

So given the strain rates as a function of time, or the strain over some time span, we can find, for each time, $m(\mathbf{x})$, the minimum of which will give the source location that best agrees with the relative rates of strain. The slip rate assuming this source location is then given by

$$\dot{s} = \frac{(\sum_{i=1}^N (\dot{\epsilon}_i(t))^2)^{0.5}}{(\sum_{i=1}^N (G_i(\mathbf{x}))^2)^{0.5}}$$

To apply this to slip on the San Jacinto fault in the Anza area, we assume that the slip is right-lateral. Computing the strains induced at PFO by slip on different parts of the San Jacinto fault (represented by a plane dipping at 82°) gives a set of unit vectors $\hat{\mathbf{b}}$ which we can compare with unit vectors $\hat{\mathbf{a}}$ estimated from the strain changes after the 2005 Anza and 2010 EMC earthquakes. We estimate the net changes using Figure 7; Table 2 gives the values. Figure 10 shows the results for source inversion; in this figure the colored areas show the acceptable regions, defined as an angle between unit vectors of 15° or less.

This plot shows that only a small region on the fault can produce strain changes with the observed ratios. Since the ratios are similar for the two cases, it is not surprising that the acceptable regions are in roughly the same place – though the slip in 2005 is much less constrained in depth than that in 2010.

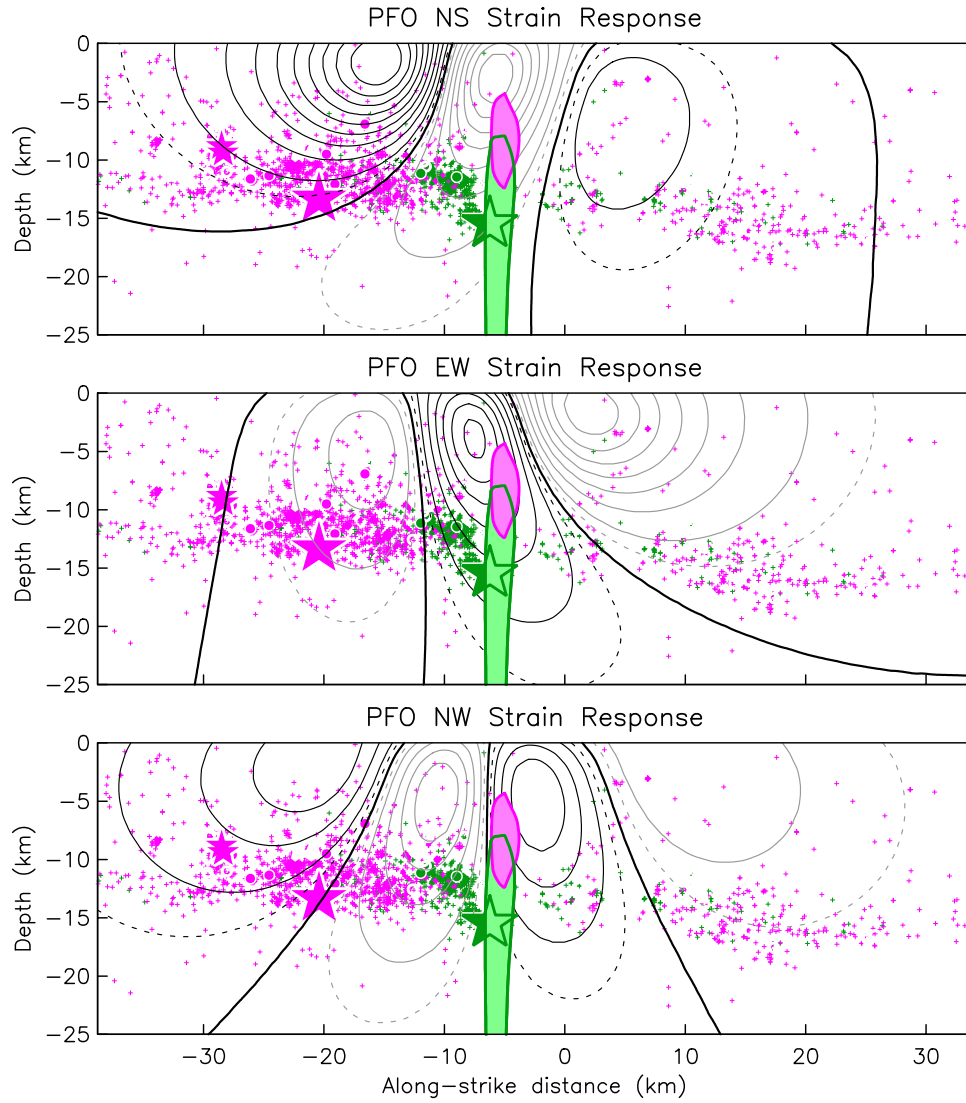


Figure 10: Side view of the San Jacinto fault, using the same coordinates as in Figure 2. The earthquakes for 2005 and 2010 are shown in magenta and green respectively. The two colored regions show where right-lateral slip would produce strain changes with the ratios derived from the values in Table 2.

If we take the fault-plane location that minimizes the angle between $\hat{\mathbf{a}}$ and $\hat{\mathbf{b}}$, we can find the total slip – or more correctly, the moment release, since we do not know the size of the source. For the 2005 aseismic strain, the moment released is 1.8×10^{17} N-m (equivalent to $M_w = 5.5$); for the 2010 strains, the value is also 1.8×10^{17} N-m. This assumes that the source areas were at the same depth; the best-fitting source location for the 2005 event is 20 km deep, which increase the distance to PFO enough to require a source about four times as large (equivalent magnitude 5.9) to give the same strain. The sources equivalent to a magnitude 5.5 event produce a maximum of 1.6 mm horizontal displacement and 2.0 mm vertical displacement on the nearest continuous GPS stations. Blind tests of detection methods (Lohman and Murray, 2013) show that motions of this size and duration would be undetectable.

7 Rapid Aseismic Strains

As noted in Section 2, the rapid strain changes seen on the PFO LSM's and BSM's following the 2013 Toro Peak earthquake (Figure 4) were not observed on any of the PBO BSM's located elsewhere in the Anza area. In order to understand this phenomenon better, we examined data from the PFO instruments over a longer span of time to see if similar events occurred at other times. A preliminary examination of the data by Prof. Peter Shearer located five similar events in 2010, eight in 2011, and nine in 2012 and 2013; however, none of these correlated with local seismicity. In this section we describe a more thorough examination of the data, aimed at using as many of these occurrences as possible to produce a composite stack which could be used for modeling of the possible source.

The first step was to develop a systematic detection method and test it against the signals Prof. Shearer had observed. Since the signal of interest was an offset lasting over one to three hours, the ideal detector would be a prediction-error filter which used data up to some time to predict the expected strain for times before and after subtracting this prediction from the observations would give close to zero for the data before the time (since these data were used to make the prediction), while the values from one to three hours later should be close to zero in the absence of an event, but nonzero if one had occurred. We examined the offsets already found on the NS LSM using three prediction methods, which fit:

1. The median of the four hours before the time of interest.
2. The mean and trend of the four hours before the time of interest.
3. The mean, trend, and two sinusoids fitting the 24 hours before the time of interest. The sinusoids used corresponded to periods of 24 and 12.42 hours, to fit the residual signals often present in the LSM data (daily thermal and possible misfits to the M_2 tide).

Of these, the third one gave the best results in terms of giving an error signal that remained constant for some time after the rapid changes; taking the mean of the residual from two to four hours after the particular time gave a good indication of the size of a possible offset over that time. Applied to the whole series after removing the predicted tides, any offsets appeared as large peaks at the time the offset began, out of what otherwise was a series varying around zero.

The next step was to scan, visually, all the LSM data from the start of 2006 through mid-2016, looking simultaneously at

- The NS LSM strain data, after removing the predicted tides, looking for abrupt positive changes (that is, changes over 1-2 hours).
- The same, with the prediction-error filter applied.

This scan produced a list of NS events, with times, durations, and approximate amplitudes. These times were used to scan the EW data to get amplitudes and durations for the events there. The net result was a list of 73 possible events, the earliest on 2007:146 and the last on 2016:043. Over the time examined by Prof. Shearer, 25 events matched, 10 were found that were not in his list, and 6 in his list were not found: all of the latter were double-checked and included if they seemed to be actual events.

In order to look more closely, all events were plotted with the prediction-error filter being used at the time chosen, to produce what should be a gradual offset starting at that time and ending in a few hours. These plots were used to grade the quality of the offset, which might not be suitable for stacking simply because (for example) temporary local instrumental instability, and also to estimate the duration and offset more precisely for those offsets graded A and B, which had a high enough quality for this to be done. Figures 11 and 12 are examples of the final version of these plots, which include, for A and B events only, the grade, and also the idealized offset assuming the estimated duration and amplitude; some iteration of these plots ensured that for the final stack only the highest-quality events would be present, with known durations and amplitudes (needed for a weighted sum).

The next check was to restrict the events to those of quality A on the NS LSM, and with durations from 60 to 90 minutes: this limited the number to 25. Then, for each dataset to be stacked, a plot was made showing each event (normalized by its amplitude) against a background of all the events. This made it possible to remove, for each dataset, examples that were outliers for that particular system. Figure 13 shows such a plot for the EW LSM, which identifies three events for which that dataset is significantly different from the others; for the final stack, these, and two of the events with no reliable amplitude from the NS LSM, were not included.

Following this tedious but necessary winnowing of the data it was possible to create reliable stacks of the data, to reduce noise and emphasize common-mode behaviour. Figure 13 shows the result. Each stack was constructed by forming the sum of all the records, and then dividing by the sum of all the amplitudes for the NS LSM, to give a weighted average. Obviously this works best for the NS data itself, but the results for the EW and NWSE LSM are also quite good. The duration of the EW events appears to be slightly longer than the NS events, almost exactly half as large, and in the opposite direction. This plot also brings out clearly that these events are hardly seen at all on the NWSE LSM: the amplitude cannot be greater than 0.05 of the NS response. It is also clear that these events are indeed offsets; at least over the eight hours shown here no decay back to the zero level is clearly obvious.

Figure 14 shows the result of applying this same process to the different channels of the PBO BSM; we have examined the data in this way, rather than the areal and shear strains constructed from

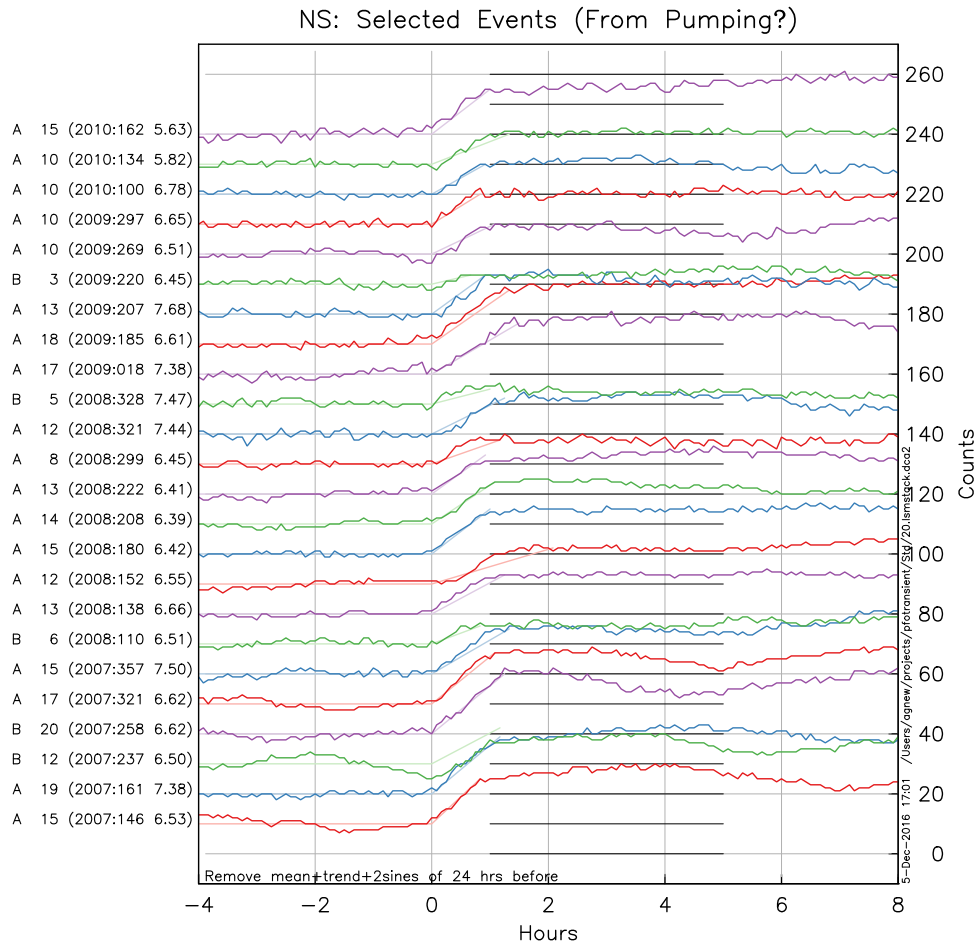


Figure 11: Quality A and B events from the NS LSM. For each event an ideal version with the specified duration and amplitude is underplotted in a light color. To the left of each trace is the grade, the amplitude, the date, and the time in terms of fractional day of the week.

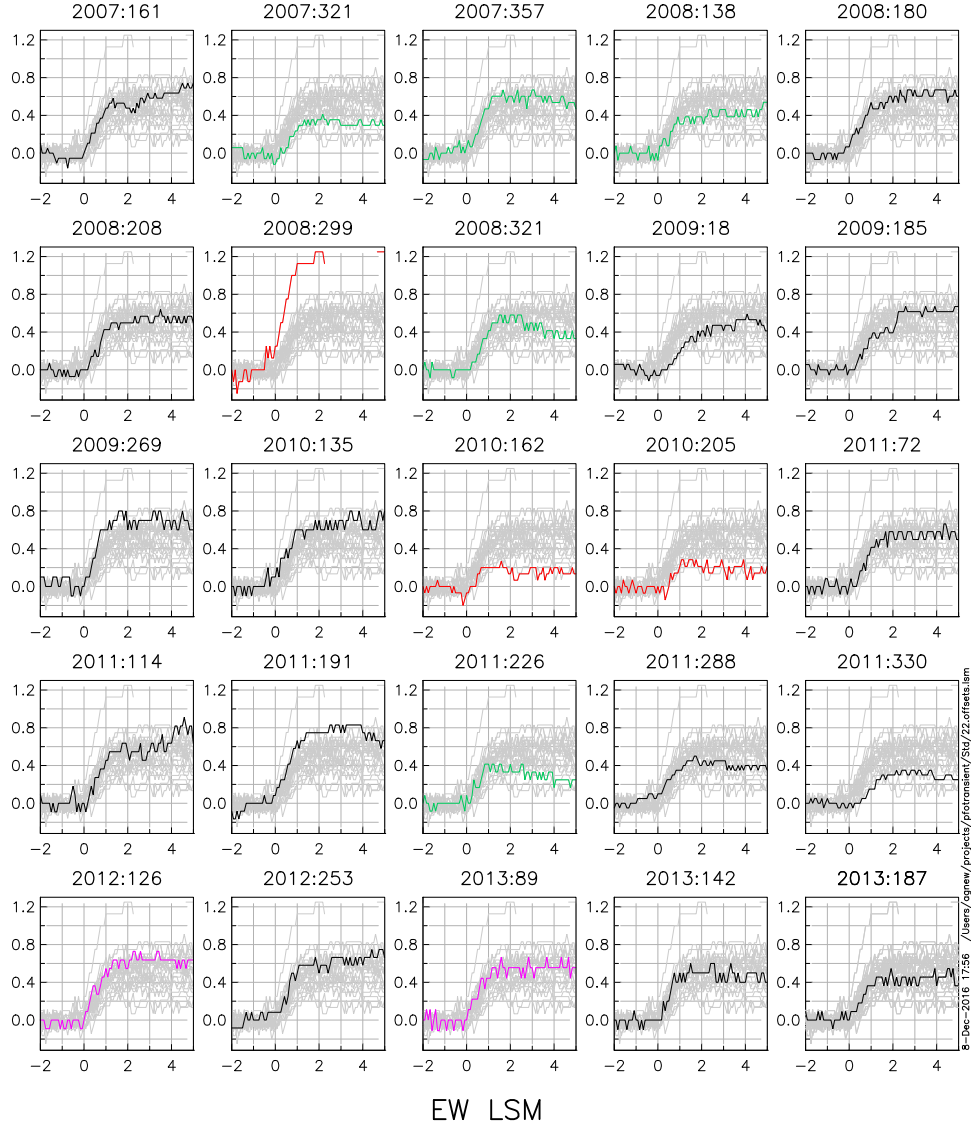


Figure 12: The events as they appear on the EW LSM, for the 25 quality-A events on the NS LSM with durations between 60 and 90 minutes. In each frame all events are plotted in gray, with the event for that particular time plotted on top: red if deemed to be an unacceptable outlier, purple if the event is unacceptable on the NS LSM, green if the event is unacceptable on some other dataset, and black otherwise. The red and purple events are not used in the final stack. In all frames, the x -axis is time in hours and the y -axis normalized amplitude.

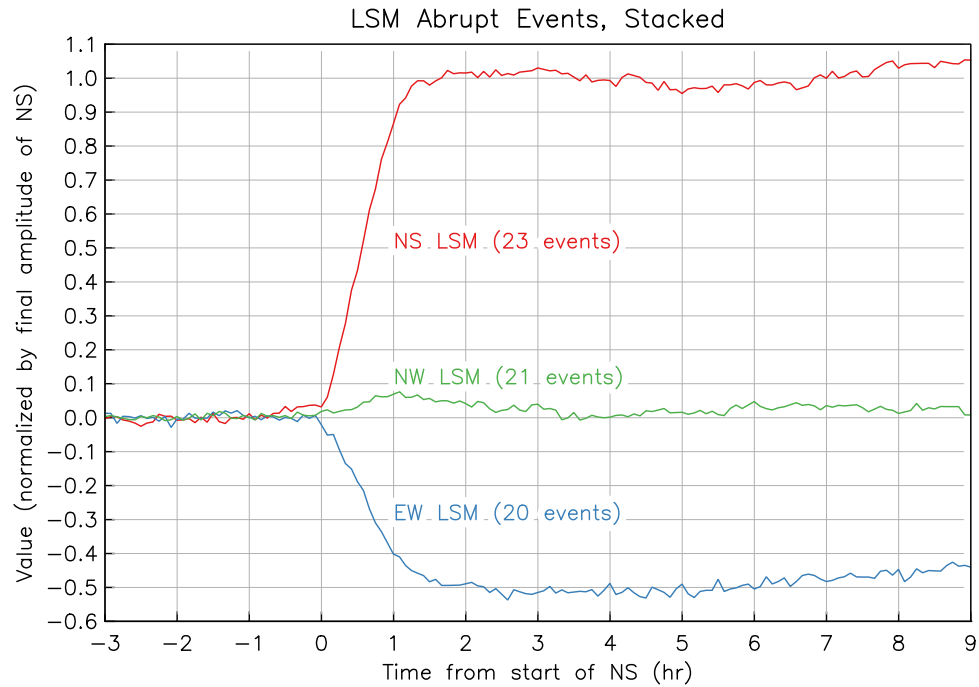


Figure 13: Stack of the LSM data for selected events; amplitudes are relative to the NS LSM being normalized to unity. The number of events in each stack is given.

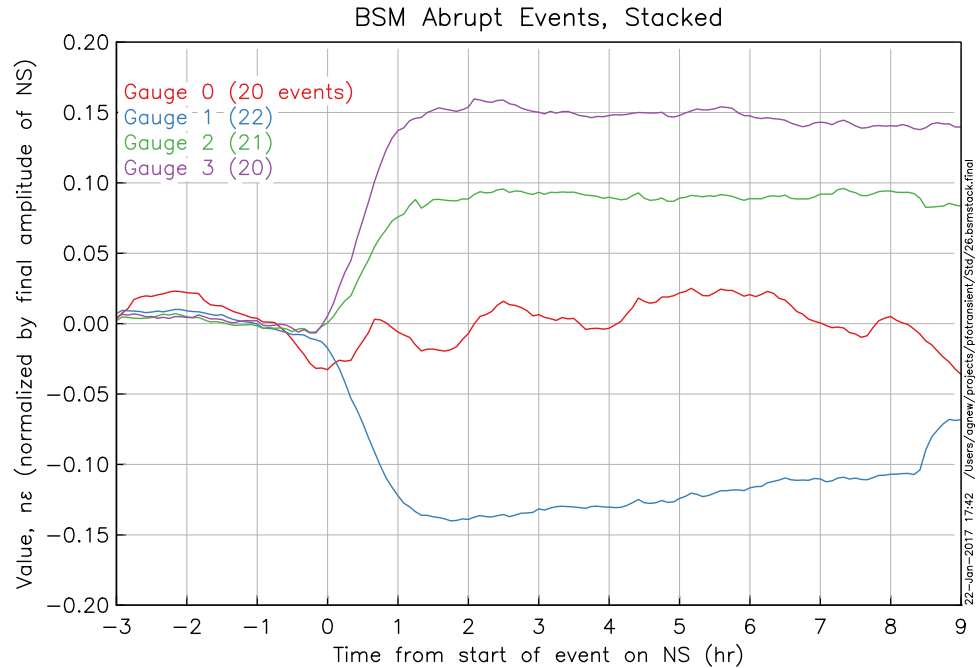


Figure 14: Stack of the four channels of the PBO BSM data for selected events; amplitudes are in nominal strain for the BSM channels, relative to the NS LSM being normalized to unity: one least count of the NS LSM, which corresponds to 2.2×10^{-9} strain.

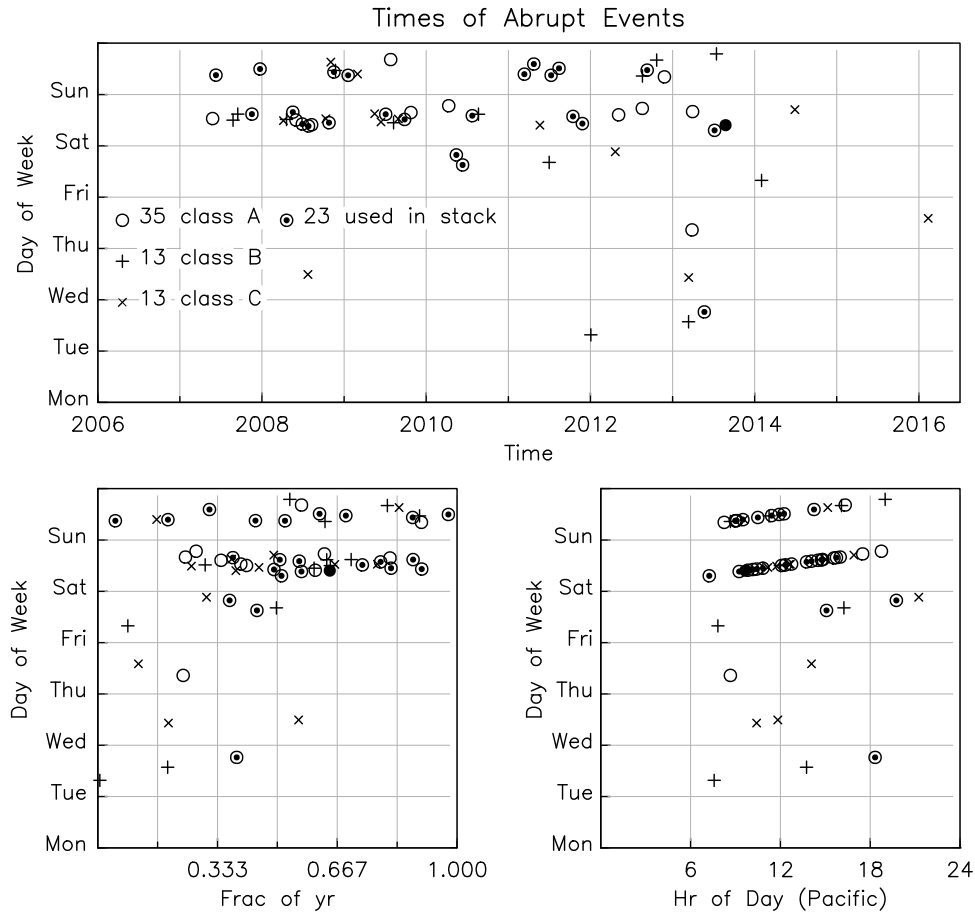


Figure 15: Times of “abrupt events” seen on the PFO strainmeters, plotted as day of the week against absolute time, time of year, and time of day; note that the slope in the last is inherent in time being used for both axes.

them, to avoid issues both with noise on one channel contaminating all the computed strains, and any calibration uncertainties. The results would appear to justify this approach, since it is clear that Channel 0 of the BSM is significantly noisier than the other three over the time periods of interest (one to four hours).

There is thus, as there was at the time of the 2013 earthquake, a consistent pattern to these short-term changes. Unhappily, we cannot attribute them to tectonic activity, because of what is shown, in Figure 15, about the time of these events. They have occurred only from 2007 through 2013 (top frame); throughout the year but rarely in December through March; virtually always during local daytime; and very predominantly on the weekends. This is very much the signature of an anthropogenic source (Agnew, 1990), specifically of someone making weekend visits to a second home during the warmer parts of the year and running a well pump when they are there. While the abrupt events in the wake of the 2013 earthquake were not on a weekend, they were during the day (for local time) and we have to assume that they were caused by the same source: local pumping rather than some novel tectonic signal.

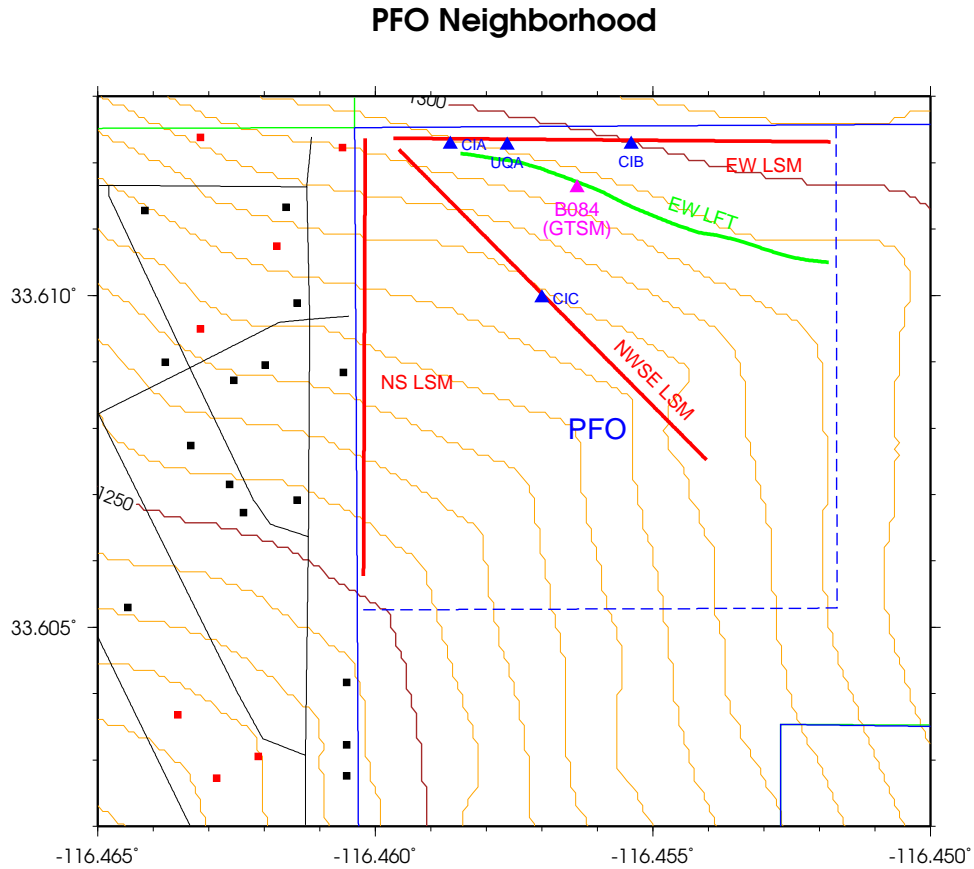


Figure 16: Map of PFO showing the locations of the different systems discussed here, along with the locations of houses in the region just to the west; those in red have been constructed since 2007 – though as elsewhere, 2008 represented the end of construction for the next five years or so.

Even though this makes this signal of less interest geophysically, it is still important to try to understand it as a possible source of noise, in the spirit of Evans and Wyatt (1984). This paper looked at how a water-table perturbation (from drilling) at PFO could cause a response on the long-base strainmeters – albeit one with a different pattern than we see here, one that was consistent with depressurization of a large horizontal fracture beneath the NW corner of the observatory. The difficulty in understanding the 2007-2013 events in this way has been indicated above: while it is possible to cause apparent strains on the LSM's by displacing all three ends that lie in this part of the observatory, it is difficult to see how this could also cause significant strain at the PBO borehole strainmeter, which is relatively far from the region where the LSM's converge: Figure 16, a map of the observatory and its neighborhood, shows the locations.

This map also shows the (relatively sparse) dwellings nearby, separating them into ones built before 2007 and ones built later,¹ since the latter are much more plausible sources for the time history shown in Figure 15. The house built directly next to the NW corner of PFO would at first seem to

¹ This information comes from the property-tax rolls maintained online in 2008 by Riverside County, updated by examining later photographs from Google Earth.

be a possibility, except that: (a) pumping from it would be likely to cause a large apparent strain on the NWSE LSM, and (b) precisely because of concerns about the effects of pumping there, we have monitored this (with the owners' permission) and know that it is not the cause – nor has this house ever been used as a weekend residence.² We are looking into the next-nearest new house (due west) to see if it has had a weekend pumping pattern over the times from 2007-2013.

Another potential source of information comes from the water-height records we collect at three boreholes at PFO; these (also shown on Figure 16) were drilled about 35 years ago and have never been pumped. The water height is sampled at a 5-minute interval and thus can be stacked just as the other data can; Figure 17 shows the results. None of the water height series show anything like the abrupt changes seen in the strain data, even though some of them (notably CIC) provide excellent recordings of the earth tides. It might at first appear that the systematic rise in water level over the six hours following each event is significant, and perhaps delayed because of diffusion effects. But this does not appear to be the case; rather, this rise seems to be caused by a similar change in barometric pressure. It might at first seem strange that the pressure would show any systematic behavior; we believe that it does because of the relatively restricted range of times at which these events occur, so which means that the atmospheric tides (Chapman and Lindzen, 1970; Ray, 2001; Ray and Ponte, 2003) interfere constructively to produce an apparent signal.

8 Conclusions

In summary, we conclude that the LSM and BSM data from PFO provide strong evidence for aseismic strains following either large regional earthquakes, or moderate shocks in the nearby Anza gap. This gap also appears to be a plausible source for these strains, implying that parts of the fault as seismogenic depths are capable of stable sliding in response to high dynamic stresses. This slip should be included in any budget of slip released and accumulated on this segment of the fault – though this additional release is certainly not enough to offset the strain accumulation shown by GPS measurements. The Anza gap thus seems even more probable as a location for a future significant earthquake, just as Thatcher *et al.* (1975) suggested. But four decades later, we are still waiting for this earthquake to arrive – a reminder that the earthquake cycle, even on the most active faults, is quite long in human terms. But even if the next Anza earthquake does not arrive for another four decades, the strain data collected at PFO has shown an interesting and unexpected phenomenon that may aid our understanding of fault mechanics.

9 Publications from the work performed under the award

None to report.

² Indeed, having been built at the very end of the housing bubble in 2008, it was derelict for some years thereafter, as the builder had gone bankrupt.

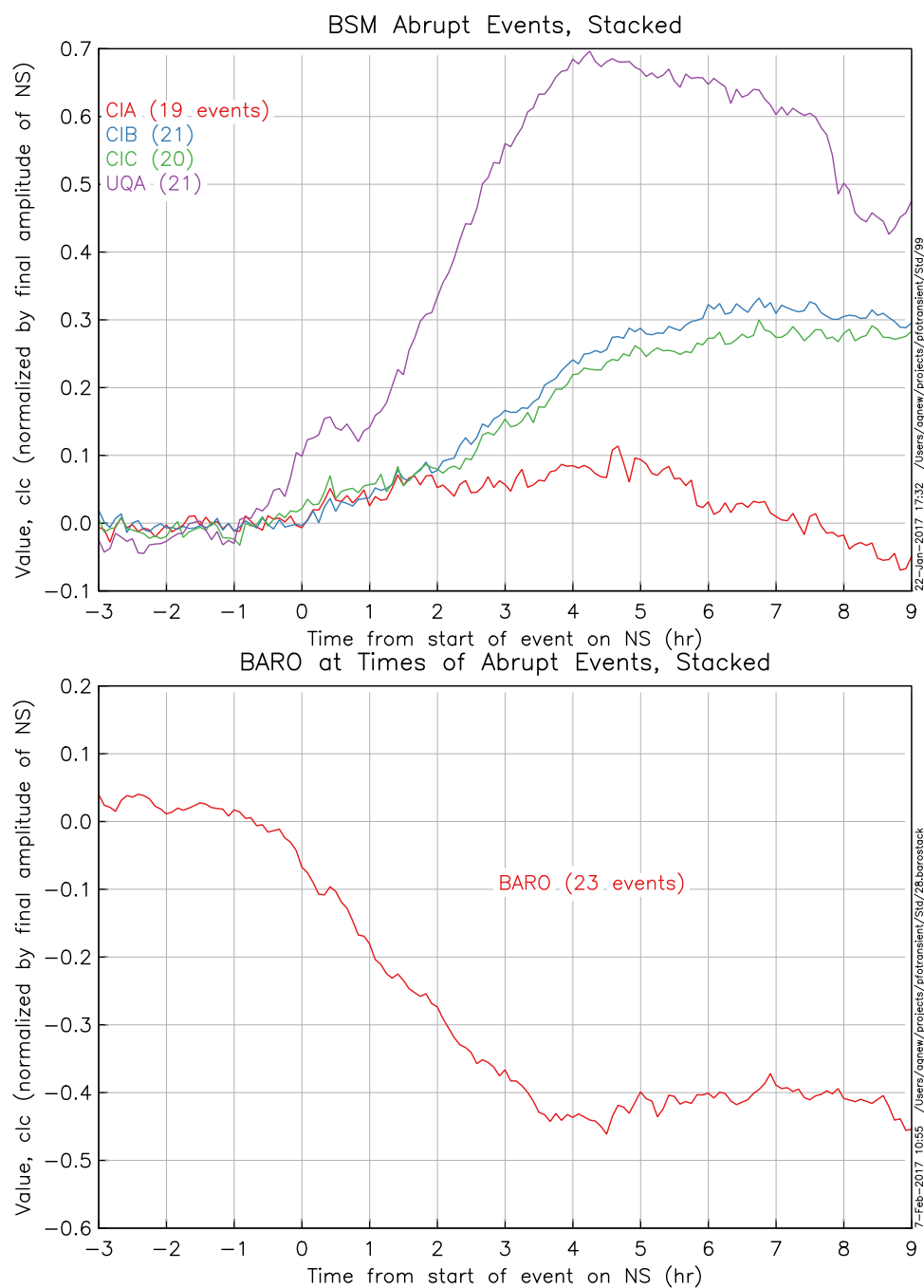


Figure 17: Stack of (top) the three water-height series and (bottom) the barometric pressure series from PFO.

References

- Agnew, D. C. (1990), The use of time-of-day seismicity maps for earthquake/explosion discrimination by local networks, with an application to the seismicity of San Diego County, *Bull. Seismol. Soc. Am.*, **80**, 747–750.
- Chapman, S., and R. S. Lindzen (1970), *Atmospheric Tides: Gravitational and Thermal*, Gordon and Breach, New York.
- Elkhoury, J. E., E. E. Brodsky, and D. C. Agnew (2006), Seismic waves increase permeability, *Nature*, **441**, 1135–1138.
- Evans, K., and F. Wyatt (1984), Water table effects on the measurement of earth strain, *Tectonophys.*, **108**, 323–337.
- Hauksson, E., W. Yang, and P. Shearer (2012), Waveform relocated earthquake catalog for Southern California (1981 to June 2011), *Bull. Seismol. Soc. Amer.*, **102**, 2239–2244, doi:10.1785/0120120010.
- Hodgkinson, K. M., J. Langbein, B. Henderson, D. Mencin, and A. A. Borsa (2013), Tidal calibration of plate boundary observatory borehole strainmeters, *J. Geophys. Res.*, **117**, 447–458, doi:10.1029/2012JB009651.
- Lohman, R., and J. Murray (2013), The SCEC geodetic transient-detection validation exercise, *Seismol. Res. Lett.*, **84**, 419–425, doi:10.1785/gssrl.84.3.419.
- Ray, R. D. (2001), Comparisons of global analyses and station observations of the S₂ barometric tide, *J. Atmosph. Solar-Terr. Phys.*, **63**, 1085–1097.
- Ray, R. D., and R. M. Ponte (2003), Barometric tides from ECMWF operational analyses, *Annales Geophysicae*, **21**, 1897–1910.
- Rockwell, T. K., G. G. Seitz, T. E. Dawson, and J. Young (2006), The long record of San Jacinto fault paleoearthquakes at Hog Lake: implications for reginal patterns of strain release in the southern San Andreas fault system, *Seismol. Res. Lett.*, **77**, 270.
- Salisbury, J., T. Rockwell, T. Middleton, and K. Hudnut (2012), LiDAR and field observations of slip distribution for the most recent surface ruptures along the central San Jacinto Fault, *Bull. Seismol. Soc. Amer.*, **102**, 598–619, doi:10.1785/0120110068.
- Sanders, C. O., and H. Kanamori (1984), A seismotectonic analysis of the Anza seismic gap, San Jacinto fault zone, Southern California, *J. Geophys. Res.*, **89**, 5873–5890.
- Thatcher, W., J. A. Hileman, and T. C. Hanks (1975), Seismic slip distribution along the San Jacinto Fault zone, Southern California, and its implications, *Geol. Soc. Am. Bull.*, **86**, 1140–1146, doi:10.1130/0016-7606(1975)86\$<\$1140:SSDATS\$>\$2.0.CO;2.
- Wdowinski, S. (2009), Deep creep as a cause for the excess seismicity along the San Jacinto fault, *Nature Geosci.*, **2**, 882–885, doi:10.1038/ngeo684.